Surface & Coatings Technology 324 (2017) 419–428

Contents lists available at ScienceDirect

Surface & Coatings Technology

journal homepage: www.elsevier.com/locate/surfcoat

Multi-method identification and characterization of the intermetallic surface layers of hot-dip Al-coated steel: $FeAl_3$ or Fe_4Al_{13} and Fe_2Al_5 or Fe_2Al_{5+x}

Antoine Van Alboom [a,*], Babs Lemmens [b,c], Benjamin Breitbach [d], Eddy De Grave [e], Stefaan Cottenier [f,g], Kim Verbeken [b]

[a] Department of Applied Physics, Ghent University, Valentin Vaerwyckweg 1, BE-9000 Gent, Belgium
[b] Department of Materials, Textiles and Chemical Engineering, Ghent University, Tech Lane Ghent Science Park – Campus A, building 903, BE-9052 Gent, Belgium
[c] Research group of Electrochemical and Surface Engineering (SURF), Vrije Universiteit Brussel (VUB), Pleinlaan 2, B-1050 Brussels, Belgium
[d] Max-Planck-Institut für Eisenforschung GmbH, D-40237 Düsseldorf, Germany
[e] Department of Physics and Astronomy, Ghent University, Proeftuinstraat 86, BE-9000 Gent, Belgium
[f] Department of Electrical Energy, Metals, Mechanical Constructions and Systems, Ghent University, Tech Lane Ghent Science Park – Campus A, building 903, BE-9052 Gent, Belgium
[g] Center for Molecular Modeling, Ghent University, Tech Lane Ghent Science Park – Campus A, building 903, BE-9052 Gent, Belgium

ARTICLE INFO

Article history:
Received 28 March 2017
Revised 11 May 2017
Accepted in revised form 31 May 2017
Available online 1 June 2017

Keywords:
Intermetallics
Density functional theory
Atom probe tomography
Electron backscatter diffraction
Mössbauer spectroscopy
Fe-Al

ABSTRACT

Until now, several different chemical formulae are used to refer to the intermetallic θ- and η-layers formed at the surface of hot-dip aluminized steel. To clear up the subsequent confusion, both layers were identified and characterized using several experimental techniques combined with DFT calculations.[1] EDX- and EBSD-mappings were performed on the cross section of a hot-dip aluminized steel and showed the presence of the two single-phased intermetallic layers, θ and η, just beneath the aluminum top-layer. The XRD-pattern of a sample of which the top aluminum layer was removed, confirmed the foregoing observations. The compositions of both layers were determined by APT and yield Fe_4Al_{13} and $Fe_2Al_{5.6}$. DFT calculations showed the stability of the Fe_4Al_{13} phase and predicted Fe_4Al_{13} to be the only stable composition in that area of the Fe-Al phase diagram. Based on the DFT results, the ILEEMS spectrum of the θ-layer could be successfully analyzed and, for the first time, fully interpreted in accordance with the crystallographic structure of Fe_4Al_{13}. Fe_4Al_{13} is suggested for referring to the composition of the θ-layer, instead of other formulae, e.g. $FeAl_3$. The ILEEMS η-layer spectrum was best reproduced by a model-independent quadrupole splitting distribution, which supports the dis-ordered structure model for the η-layer. An analysis based on the results of the DFT calculations, confirmed this finding. Because of the partially dis-ordered structure of the η-layer and the width of the related region in Fe-Al phase diagrams, Fe_2Al_{5+x} is suggested for referring to the composition of the η-layer.

1. Introduction

Hot-dip aluminizing is an economical and versatile technique to apply an aluminum coating to steel. During this process, inter-diffusion of aluminum and iron leads to the formation of Fe-Al intermetallic phases. Because the nature of these phases determines the properties of the end product, e.g., mechanical brittleness or electrochemical behavior, an unambiguous determination of the structure and composition of these phases is essential for the understanding and the development of new applications. Although there is a long tradition of research into the characterization and understanding of these phases, there is still a fair amount of confusion concerning the composition, as will be pointed out hereinafter.

The study of Fe-Al alloys in the context of coatings started with the work of Heumann and Dittrich [1] in 1959. For a hot-dip aluminized Fe sample, they showed the presence of an intermetallic layer with an orthorhombic structure, which grows in a fingerlike manner into the iron and which is nowadays known as the η-layer. They attributed the Fe_2Al_5 stoichiometry to this phase, based on preceding XRD measurements and structure refinement by Schubert [2] for bulk samples. Later, Burkhardt et al. [3] refined this structure for single-crystal fragments selected from a crushed alloy with stoichiometry $Fe_{28.5}Al_{71.5}$ ($\approx Fe_2Al_{5.02}$). Their refinement was carried out in the Cmcm space group, and led to an orthorhombic structure with stoichiometry

* Corresponding author.
E-mail address: toon.vanalboom@ugent.be (A. Van Alboom).

[1] EDX: energy dispersive X-ray spectroscopy; APT: atom probe tomography; EBSD: electron backscatter diffraction; XRD: X-ray diffraction; ILEEMS: Integral Low-Energy Electron Mössbauer spectroscopy; DFT: density functional theory.

http://dx.doi.org/10.1016/j.surfcoat.2017.05.091
0257-8972/

$Fe_2Al_{5.6}$ (ICSD 105132, COD 2106083). Burkhardt et al. [3] demonstrated that the η-phase is partially disordered, with sparsely occupied 4b and 8f Al sites. Published phase diagrams [4,5,6] for the Fe-Al system show a rather narrow homogeneity range for the η-phase. In a recent re-evaluation of this phase diagram by Li et al. [5], the homogeneity range of the η-phase has been determined to cover the interval from $Fe_2Al_{4.67}$ to $Fe_2Al_{5.30}$. On the other hand, Han et al. [6] determined the lower limit of this interval at $Fe_2Al_{4.37}$. These findings are not entirely consistent with the refinement by Burkhardt et al. [3]. In the coating literature, the name 'Fe_2Al_5' is commonly used to indicate the η-phase [7,8,9,10], although occasionally Fe_4Al_{11} [11] or $Fe_2Al_{5.4}$ [12] appear as well. Because names with integer stoichiometry incorrectly suggest a well-defined composition, the name Fe_2Al_{5+x} will be used in this work. Therein, x can be negative or positive. Following Li et al. [5], x is lying between −0.33 and 0.30. Following Han et al. [6], x is lying between −0.63 and 0.30.

Eggeler et al. [13] showed that apart from the dominant η-layer, also a minority phase is formed after hot dipping. It manifests itself as a thin layer that separates the η-phase from the top aluminum layer, and is now known in the coating literature as the θ-phase. Using selected area diffraction transmission electron microscopy, they identified this phase as $FeAl_3$. Many other authors [14,15,16,17,18,19,20] also use the designation $FeAl_3$ for the composition of the θ-phase. However, following Black [21] and Grin et al. [22], the actual stoichiometry is Fe_4Al_{13} (ICSD 151129). There seems to exist a general consensus about its monoclinic structure with space group C2/m. Until now, the name "$FeAl_3$" has continued to be the most commonly used one for this phase in the coating literature, and it appears even in reference works for binary phase diagrams, see e.g. [23,24,25]. Table 1 summarizes some crystallographic characteristics of the η- and θ-phases as indicated in literature.

In the past, η- and θ-phases also were investigated by conventional transmission ^{57}Fe Mössbauer spectroscopy (CTMS) and conversion electron Mössbauer spectroscopy (CEMS) by several authors for bulk samples [26,27] and in surface layers [28,29]. Different models have been proposed to analyze the observed Mössbauer spectrum of the Fe_4Al_{13} (or "$FeAl_3$") θ-phase, using, e.g., the superposition of three single spectral lines with independent parameters [26] or one spectral quadrupole doublet combined with two independent singlets [28]. However, in none of these attempts, a physically justified relation between the Fe sites in the structure and their occupation on the one hand, and the assignment of the various spectral components and their relative areas on the other hand, has been established. Concerning the η-phase, Mössbauer spectra reported in the literature and referring to that phase [27,28,29] were analyzed with one spectral quadrupole doublet. In all cases the adjusted doublet exhibited similar Mössbauer parameters, and was assigned to one unique Fe site by the cited authors. However, the occurrence of one unique Fe site is not consistent with the variability in local environments due to the partial occupancy of the Al-8f and Al-4b sites in partially disordered Fe_2Al_{5+x} [3]. This discrepancy has never been addressed in studies related to the analysis of observed Mössbauer spectra.

In the present work, a multi-method investigation of a set of similarly produced hot-dip aluminized steel samples has been undertaken. By the consistent analysis of information from experimental methods sensitive to either the composition, crystal structure or both, combined with density functional theory (DFT) calculations, unambiguous conclusions have been obtained about the intermetallic phases that appear in hot-dip aluminized steel, and their relation to the equilibrium bulk phases.

2. Method overview

In this section, the techniques used in this work to characterize and identify thin intermetallic layers in a hot-dip aluminized steel are concisely discussed.

A scanning electron microscope (SEM) to which an EDX (energy dispersive X-ray spectroscopy) detector is coupled, makes it possible to distinguish the different layers in a cross section image of the sample. However, application of EDX for the determination of the composition of the intermetallic layers is not straightforward. Due to pear-shaped penetration depth of the electrons, the material underneath the Fe-Al layers will contribute as well, inducing a compositional error. Additionally, the chemical compositions of the η- and θ-phases differ only little, which makes it difficult to distinguish them in the secondary electron (SE) mode.

Atom probe tomography (APT) is a material characterization technique that allows to obtain 3D information on the material with subnanometer spatial resolution (around 0.1–0.3 nm resolution in depth and 0.3–0.5 nm laterally). Information on the chemical identity of the analyzed ions allows to gather information on the structure of the material on an atomic level. Although the sample preparation is very tedious, it is able to provide additional insights as compared to the more traditional EDX analysis [30].

Conventional X-ray diffraction (XRD) enables to identify the different phases in the intermetallic layers of the specimen since the penetration depth is large enough (>10 μm) to probe all of them, provided that the outer Al layer has been removed first.

Electron backscatter diffraction (EBSD) is applied to confirm the identification of the different phases present, based on the determination of their crystallographic structure and on their orientation in the material. In EBSD, the incident electron beam of the SEM is diffracted by the atomic layers of the sample, thus producing a diffraction pattern that is characteristic of the crystal structure and orientation of the sample region from which it was generated. The penetration depth can vary between ca. 10 and 100 nm, depending of the accelerating voltage of the electron beam and the atomic numbers of the atoms in the sample [31]. The technique was already used for the indexing of the EBSD pattern of "$FeAl_3$" [16] and for the investigation of the crystallography of "Fe_2Al_5" [10].

For identification of Fe-containing phases specifically, ^{57}Fe Mössbauer spectroscopy is a common and widely used technique. Conventional transmission ^{57}Fe Mössbauer spectroscopy (CTMS) is based upon the recoilless nuclear resonance absorption of 14.4 keV gamma photons by ^{57}Fe nuclei embedded in solids. ILEEMS (Integral Low-Energy Electron Mössbauer Spectroscopy) and CEMS (Conversion Electron Mössbauer Spectroscopy) are emission variants of CTMS and are both particularly appropriate for the study of surfaces. Both CEMS and

Table 1
Selection of crystallographic characteristics of the η- and θ-phases as indicated in literature.

Phase	Stoichiometry cited	At.% Al	Lattice parameters				Space group	Ref.
			a (nm)	*b* (nm)	*c* (nm)	β (°)		
η	$Fe_2Al_{5.6}$ $Fe_{28.5}Al_{71.5}$ Fe_2Al_5	73.7(6)	0.76559(8)	0.64154(6)	0.42184(4)	90	Cmcm	[3]
η	Fe_2Al_5	72.8(2)	0.7657(2)	0.6404(2)	0.4229(1)	90	Cmcm	[5]
θ	Fe_4Al_{13}	76.5(1)	1.5492(2)	0.8078(2)	1.2471(1)	107.69(1)	C2/m	[22]
θ	Fe_4Al_{13}	75.8(1)	1.5496(5)	0.8052(6)	1.2477(8)	107.69(4)	C2/m	[5]

ILEEMS are based on the detection of resonant electrons emitted by after effects following the decay of an excited ^{57}Fe probe nucleus in the studied material after resonant absorption by that nucleus of an incident 14.4 keV γ-photon. In the case of CEMS, these electrons are conversion electrons, while in ILEEMS they concern low-energy electrons (~10 eV), mostly so-called shake-off electrons. As a consequence of this low energy, only an extremely thin surface layer with a thickness of a few nanometers (~5 nm) of the material is preferentially probed by ILEEMS [32]. Therefore, the ILEEMS technique, more than CEMS, is expected to be very helpful for the characterization of the intermetallic layers at the surface of hot-dip Al-coated steel in particular. With the help of DFT calculations, the spectral components resolved from the experimental ILEEMS spectra may then be related to particular Fe sites in the respective structures, making the explanation of their parameters more sound and reliable.

Density functional theory (DFT) is a formalism to solve the many-body Schrödinger equation. It is in principle exact, approximate in practice, and it can be routinely applied to crystals with 100 or more atoms in the unit cell. DFT provides results that are in many cases close to the experimental values [33,34,35,36,37]. The primary result of a DFT calculation is the ground state total energy of a crystal, from which the formation energy of the crystal can be obtained as the difference with the total energy of the elementary phases. In this way, ground state phase diagrams as a function of concentration can be computed [38], which has indeed been done in the case of the Fe-Al phase diagram [39]. Further, for a given crystal structure, Mössbauer parameters can be predicted from DFT as well [40,41]. When these calculated parameter values agree with experimental Mössbauer parameters for a sample with a not yet determined phase, the crystal structure of that sample can be assessed [42]. DFT predictions for the Fe-Al phase diagram and Mossbauer parameters obtained by DFT will be used in this work to unambiguously associate the Mössbauer experimental results to the involved Fe-Al crystal structures.

3. Sample production, experimental and computational procedures

The steel substrate was aluminized with a Rhesca® hot-dip simulator by immersing a 1.2 mm thick low carbon steel (0.04 wt% C; European grade DC06; composition: Fe-0.01C-0.015Si-0.1Mn-0.01Cr-0.018Ni-0.05Al-0.01Cu-0.04Ti) in an aluminum bath containing 3 wt% iron, under a reducing atmosphere (nitrogen with 5 vol% hydrogen). The aluminum bath was saturated with iron to keep dissolution of the steel during dipping to a minimum [13]. The steel plate was heated to 800 °C for 60 s and then dipped in molten aluminum for 60 s at a bath temperature of 680 °C. After dipping, the aluminized sheet was cooled to room temperature with nitrogen gas.

SEM investigations were done with a FEG (field emission gun) SEM Quanta 450 apparatus equipped with a TSL EBSD and an EDX system.

APT measurements were performed using a local electrode atom probe (ImagoLEAP™ 3000X HR) operating in laser mode under ultra-high vacuum. Set point temperature of 60 K, pulse repetition rate of 250 kHz, laser energy of 0.2 nJ and a detection rate of 0.01 atoms per pulse were used as experimental APT parameters. APT data were reconstructed and analyzed within the framework of the IVAS® software. The sample was prepared as described in [30].

For the ILEEMS measurements, the intermetallic layers have to be uncovered. For the XRD, only the outer Al-layer has to be removed. To target the θ-layer, the upper aluminum layer was removed by electrolytic etching as described in Lemmens et al. [43]. For this an Ametek Versastat 4 potentiostat was used in a three electrode set-up. The hot-dip aluminized (HDA) steel was placed in a flat cell and served as the working electrode. A saturated Ag/AgCl electrode and a Pt grid were used as reference electrode and counter electrode, respectively. Next, the potential was held at −0.3 V vs Ag/AgCl for 20,000 s while it was in contact with a 0.1 M NaCl solution. This potential was chosen because it is lower than the breakdown potential of Al (and thus will dissolve the Al) but higher than the breakdown potential of the intermetallic phases (which as such remain intact). This procedure exposed the θ-layer. To target the deeper lying η-layer of the HDA steel, the outer aluminum layer and the θ-layer were mechanically removed by grinding and polishing.

XRD measurements were performed using a Philips PW1830 diffractometer, equipped with a cobalt X-ray source (Co K_α radiation $\lambda = 0.17889$ nm) working with a voltage of 40 kV and a current of 30 mA. The diffractometer setup was a Bragg-Brentano geometry with slits (primary side 1°/secondary side 0.2°), a flat graphite monochromator on secondary side and point detector. The measurements were done as a symmetrical scan for 2θ angles between 10° and 119.5° with a step size of 0.02° and a count rate of 10s/step. During counting, the sample was rotated around the sample normal to improve the statistics (10 loops/step). Fundamental parameter fits were done applying the Pawley method [44].

ILEEMS spectra at room temperature (RT) of the samples with uncovered θ- and η-phases, respectively, were recorded with the respective samples and the electron detector (channeltron) both mounted in a vacuum chamber. The channeltron was subjected to a bias voltage of +146 V. The spectrometer operated in the constant acceleration mode with a triangular reference signal and had excellent linearity. A ^{57}Co(Rh) source was used, but center shift values quoted hereafter are referenced with respect to α-Fe at room temperature. The measurements were run for several days until a background of at least 5.0×10^4 counts per channel was reached. For both spectra, the velocity (v) increment per channel was 0.0143 ± 0.0001 mm/s. The line width Γ (full width at half maximum) of the innermost lines of the calibration spectrum of an enriched ^{57}Fe foil was 0.253 ± 0.002 mm/s.

DFT calculations were performed with the Augmented Plane Wave plus local orbitals (APW + lo) method [45,46,47] as implemented in the WIEN2k code [48], using the Perdew-Burke-Ernzerhof (PBE) exchange-correlation functional [49]. Muffin tin radii were chosen to be 2.13 a.u. for Fe and 1.83 a.u. for Al, throughout. The basis set was determined by a plane-wave cut-off vector of K_max = 7.5 / (RMT^min = 1.83), and k-point meshes were safely converged. When constructing the unit cells, the slight aluminum deficiency in the Al_2-site of Fe_4Al_{13} was neglected (fractional occupancy of 0.92 [22]). For non-stoichiometric and partially disordered Fe_2Al_{5+x}, an ordered model was built with 4 Fe and 11 Al atoms in the primitive unit cell. The model has space group C2/m, with the former Fe-4c at two independent Fe-4i sites and the former Al-8g at two independent Al-8j sites. The partially occupied former Al-8f and Al-4b form a disordered slightly wiggling chain, that is replaced in the model by a repetitive chain of Al-atoms at alternating distances of 2.755 Å and 2.994 Å with angles that deviate 11° from a straight line (Al-4i and Al-2a). A cif file of the fully optimized unit cell is added to the Supplementary material. The two non-equivalent Fe co-ordinations allow for two different sets of Mössbauer parameters, and sample the distribution of Mössbauer parameters that is expected in this partially disordered crystal. This crystal model has a stoichiometry of $Fe_2Al_{5.5}$ that is close to $Fe_2Al_{5.6}$ that was determined by Burkhardt et al. [3], yet outside the upper end of the homogeneity range determined to be $Fe_2Al_{5.30}$ [5,6]. This implies that the disordered wiggling Al-chain is somewhat more sparse than proposed by Burkhardt et al. Yet, the ordered $Fe_2Al_{5.5}$ model used in this work, still captures the essential features of the actual Fe_2Al_{5+x} structure.

4. Results and discussion

4.1. DFT results

Fig. 1 shows the ground state phase diagram predicted by DFT, obtained from all 16 formation energies calculated in this work. It is essentially identical to the DFT-based phase diagram published by Mihalkovic and Widom [39], but it considers a few additional phases. The predicted stable phases in this diagram turn out to be Fe_4Al_{13} (θ), $FeAl_2$ and FeAl.

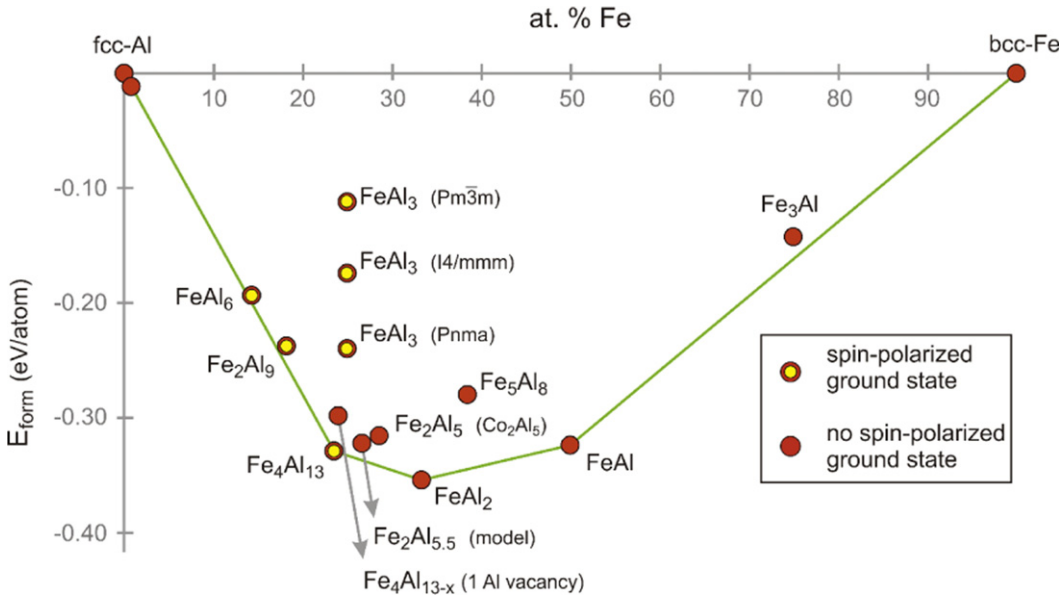

Fig. 1. DFT-predicted ground state phase diagram of the Fe-Al system. The convex hull (green) connects three thermodynamically stable intermetallic phases. Phases where the ground state is predicted not to be spin-polarized, are marked differently. Several common crystal structures for the 1:3 stoichiometry are tested, none of them being stable.

The $Fe_2Al_{5.5}$ model for Fe_2Al_{5+x} (η) lies only 20 meV/atom above the tie line, which is certainly not incompatible with its existence at room temperature. Most phases with a Fe-concentration below 25 at.% are non-magnetic, while most of those with >25 at.% are magnetic. Fe_4Al_{13} appears to lie at the transition between the magnetic and non-magnetic regime. It is non-magnetic itself, but magnetism can be induced by removing one Al-atom from its unit cell. Based on this computed phase diagram, it is reasonable to expect the occurrence of the θ- and η-phases when a Fe-surface is brought into contact with a lot of aluminum. However, the $FeAl_2$ phase would be an equally plausible candidate too.

4.2. SE, EBSD, XRD and APT results

A SE-image of a cross section of the HDA steel is presented in Fig. 2 and shows the microstructure found in inter-diffusion experiments [13,50,51], i.e.: firstly, an outer aluminum layer (ca. 5–10 μm thickness), secondly, a first intermetallic layer (ca. 5–10 μm thickness), and thirdly, a second intermetallic layer (ca. 10 → >50 μm thickness), featuring finger-like protrusions into the steel.

Fig. 3 shows different EDX mappings of Al and Fe, after hot-dipping. The Al-density is represented in blue (more blue means more Al). It can

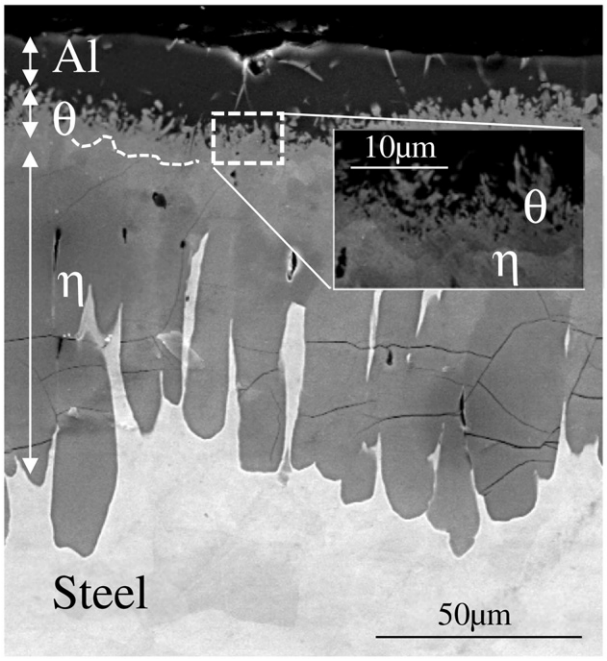

Fig. 2. SE-image of a cross section of hot-dip aluminized steel with indication of the layers.

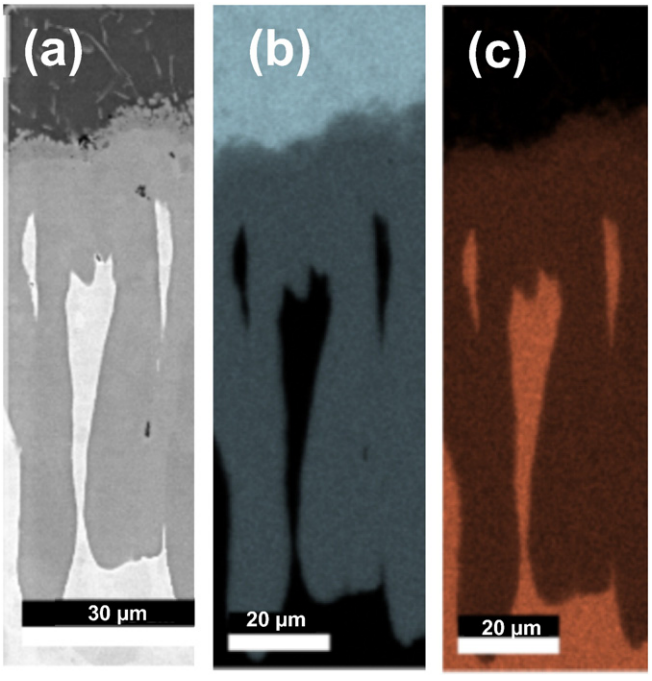

Fig. 3. EDX-mappings on a small cross section of hot-dip aluminized steel. a: steel; b: Al (blue); c: Fe (brown).

be seen that the aluminum density is high in the outer aluminum layer, smaller in the intermetallic layers, and negligibly small in the steel substrate. The opposite trend can be observed for the iron density. As the Al/Fe-ratio is very similar in the two intermetallic phases, it is not possible to distinguish them in the EDX mappings. As already mentioned in the method-overview section, due to the pear-shaped penetration depth of the electrons, also the material underneath the Fe-Al layers contributes to the composition determined by EDX, by which an accurate determination of the composition of the intermetallic layers by EDX is not possible.

To distinguish the phases, EBSD measurements were performed on the cross section of the HDA steel (Fig. 4). The contrast between the two intermetallic layers can clearly be observed in the phase map at the left hand in Fig. 4, where the aluminum is depicted in blue, the θ-phase in yellow, the η-phase in green and iron (α) in red, and which shows that the intermetallic layers are single-phased. The EBSD measurements confirm that the first intermetallic layer, just below the Al top layer, is the θ-phase, and the second intermetallic layer, just below the former one, is the η-phase, with the θ-phase being somewhat less Fe-rich than the η-phase. On the right hand in Fig. 4, the inversed pole figure of the different layers is depicted. Following the color code at the right in Fig. 4, and since all of the grains have a reddish color, it can be concluded that the [001] crystallographic direction (parallel to the normal direction) is the preferred orientation in the η-layer, which means that the η-layer is strongly textured.

In the XRD pattern of the sample of which the top aluminum layer was removed (Fig. 5), both intermetallic phases could be identified, indicating the presence of Fe_4Al_{13} and Fe_2Al_{5+x} in the two intermetallic layers of the present hot-dipped steel substrate. On top in Fig. 5, the diffractogram of Fe_4Al_{13} according to Grin et al. [22] is superimposed on the experimental one, and similarly at bottom of the drawing, the same is done for the $Fe_2Al_{5.6}$ pattern according to Burkhardt et al. [3]. With Bruker software AbsorbDX, the penetration depth of the XRD beam can be calculated for a Fe sample. This yields ca. 2 μm at an incidence angle of 5° and ca. 22 μm at an incidence angle of 60°. Because the thickness of the intermetallic layers in the present HDA sample is globally at least ca. 20 μm between protrusions at right angles to the surface (see Fig. 2), it is not surprising that reflections of the steel substrate are not observed.

Combined with the conclusion from EBSD that the intermetallic layers are single-phased, the XRD suggests that the less Fe-rich intermetallic θ-layer is Fe_4Al_{13} and the more Fe-rich intermetallic η-layer is Fe_2Al_{5+x}. Although $FeAl_2$ has been detected in Fe-Al intermetallic coatings fabricated by mechanical alloying [52], it is not detected in the present sample, neither by EBSD, nor by XRD. This does not entirely exclude its presence, as this phase could be present close to the steel side of the intermetallic phases, but might be too thin to be detected with the used material characterization techniques.

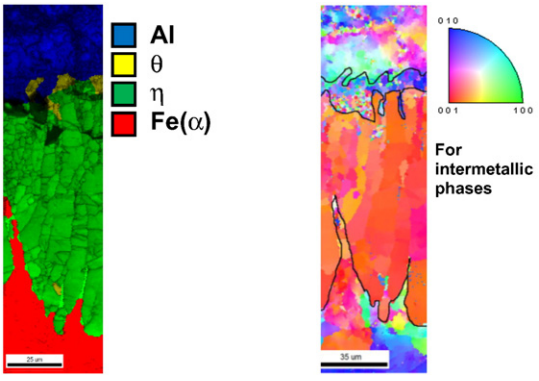

Fig. 4. EBSD mapping (left), showing the different phases present in hot-dip aluminized steel, and inversed pole figure map (right), showing the [001] crystallographic direction (parallel to the normal direction) as being the preferred orientation in the η-layer.

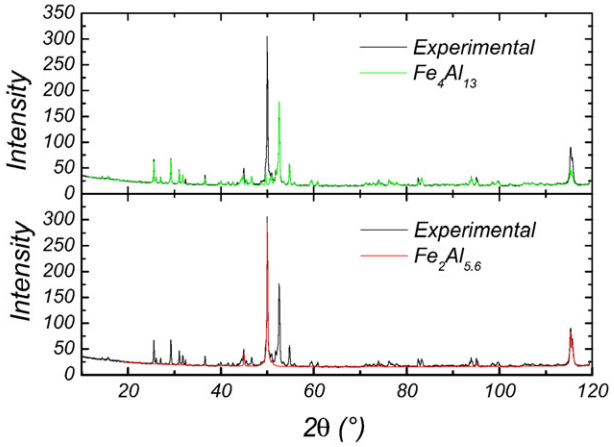

Fig. 5. XRD spectrum of hot-dip aluminized steel with uncovered θ-layer. On top: experimental spectrum with Fe_4Al_{13} diffractogram according to Grin et al. [22] superimposed. At bottom: experimental spectrum with $Fe_2Al_{5.6}$ diffractogram according to Burkhardt et al. [3] superimposed.

The composition of the intermetallic phases could be determined accurately by APT. Besides Al and Fe, the presence of <0.3 at.% Si, due to the technical purity level of the used initial materials for the synthesis, was detected. Based on APT measurements [30] and normalized to 100 at.% Fe-Al, the compositions (all hits, decomposed peaks) were derived to be 76.2 ± 0.1 and 73.7 ± 0.1 at.% Al for the θ-layer and η-layer, respectively.

The value for the θ-layer agrees very well with the ideal at.% value for Al in the chemical formula of Fe_4Al_{13} (76.5 at.% Al) and the values as determined by Black [21] and Grin et al. [22]. On the other hand, the value for the η-layer is in exact agreement with the one for $Fe_2Al_{5.6}$ determined by Burkhardt et al. [3]. Although, as mentioned in the introduction, $Fe_2Al_{5.6}$ falls just outside the homogeneity range for the η-phase in the Fe-Al phase diagram presented by Li et al. [5] and Han et al. [6], the data for $Fe_2Al_{5.6}$ of Burkhardt et al. [3] are commonly used for the characterization of the η-phase since 1994. In combination with the present APT data, this suggests that the homogeneity range for the η-phase in these phase diagrams might be somewhat too small.

4.3. ILEEMS analysis

4.3.1. ILEEMS on the sample with exposed θ-layer

ILEEMS measurements were done on the samples with uncovered θ- and η-layer, respectively. Since ILEEMS is strictly surface sensitive, no mixed spectra are expected for these layered samples. Fig. 6 presents the experimental ILEEMS spectrum for the θ-layer. The shape of this spectrum is very similar to the CTMS spectrum measured by Preston and Gerlach [26] for pure Fe_4Al_{13} synthesized by melting pure Al together with ^{57}Fe enriched Fe in an argon arc furnace (see left inset of Fig. 6, in which the full lines represent the calculated global spectrum and subspectra based on the results of Preston and Gerlach [26] against the present ILEEMS spectrum), and the CEMS spectrum measured by Prudêncio et al. [28] for a sample that was obtained by Fe ion-implantation in Al (see right inset of Fig. 6). Therefore, the present ILEEMS experiments independently support the conclusion from the EBSD experiments that the composition of the θ-phase, the top layer of this particular sample, is indeed Fe_4Al_{13}.

Preston and Gerlach [26] could propose only a merely phenomenological fit of the observed spectrum of their Fe_4Al_{13} sample, which is understandable considering the inherent complexity of the Fe_4Al_{13} structure, containing five non-equivalent Fe-positions, each of which contributes with a doublet component to the total spectrum. Each of

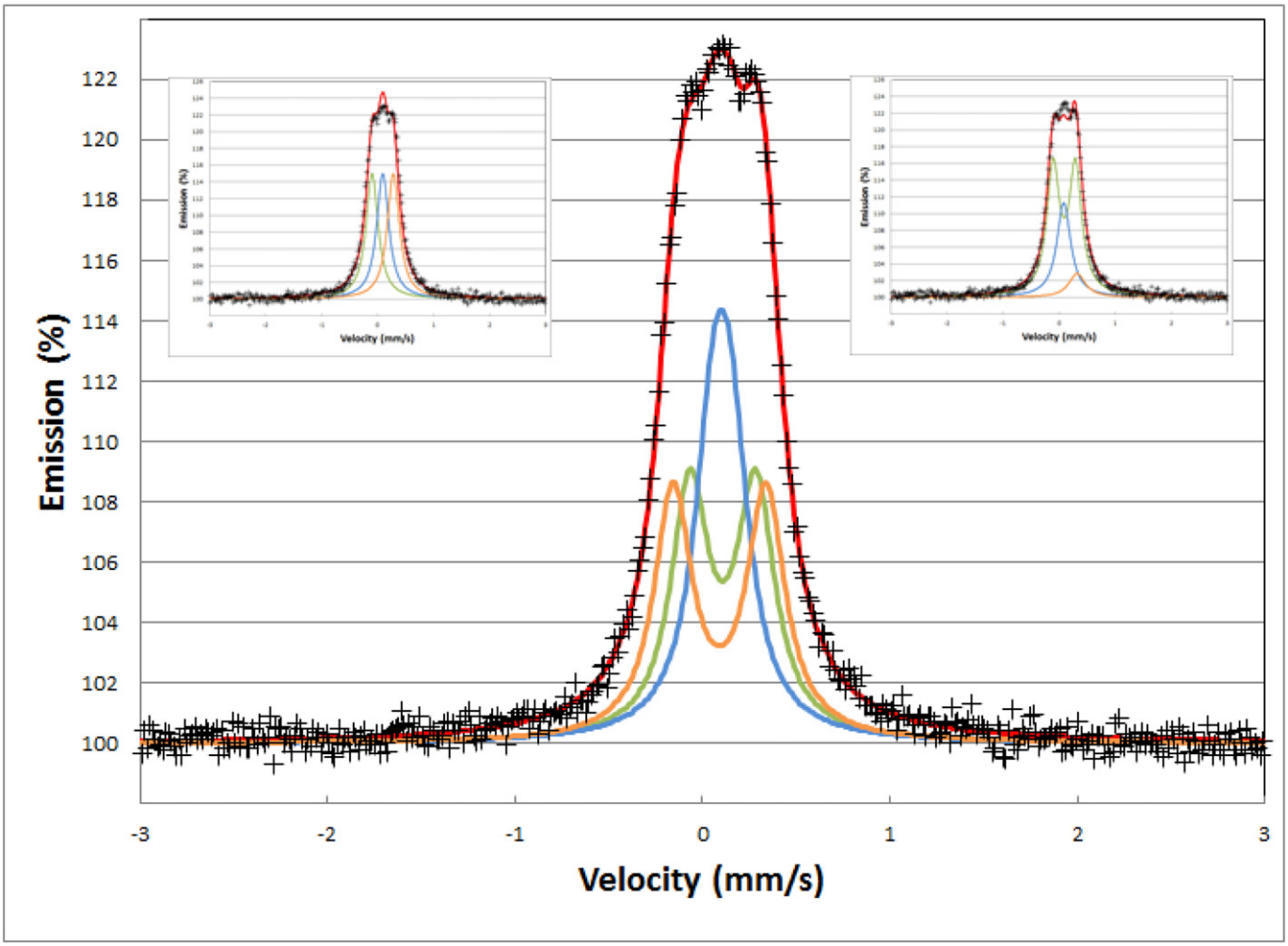

Fig. 6. Experimental (crosses) and calculated (red solid line) ILEEMS spectra for the θ-layer. Green, blue and orange solid lines represent the resolved doublet subspectra D12, D34 and D5, respectively. Doublet parameters are given in Table 3. The left inset shows calculated spectra according to the approach suggested by Preston and Gerlach [26] and the right inset shows a calculated spectrum following the suggestion by Prudêncio et al. [28], each applied to the present experimental spectrum.

these doublets is characterized by its quadrupole splitting ΔE_Q (separation between the two peaks and related to the quadrupole interaction) and by its own center shift δ (position of the center of the doublet with respect to zero source velocity). Hence, there are too many degrees of freedom to enable the determination of all the involved Mössbauer parameters from one single spectrum, the rather narrow line shape of which indicating that these five doublets are strongly overlapping. However, based on DFT calculations, predictions for the respective quadrupole splitting and center shift values can be obtained, thus possibly facilitating the analysis of the ILEEMS spectrum. These DFT-predicted values for the Mössbauer parameters of all five sites are listed in Table 2, together with the relative site abundancies (obtained from the multiplicity of each non-equivalent site). The largest quadrupole splitting in this table corresponds to an electric field gradient $V_{zz} = 2.6\ 10^{21}$ V/m^2. Following the analysis of Errico et al. [36], this is a small quadrupole interaction, and the DFT prediction can be 30% away from the true value. The predicted quadrupole splittings in Table 2 therefore point out in the first place a relative trend, rather than claiming to predict definite values.

Table 2
Mössbauer parameters, as suggested by DFT calculations, of the five quadrupole doublets (Di, $i = 1,\ldots,5$) expected to constitute the spectrum of the θ-layer and related to the five Fe sites in the Fe_4Al_{13} structure [22]. δ: center shift; ΔE_Q: quadrupole splitting; *RA*: relative area. D1, …, D4 refer to the four Fe sites with point symmetry *m*, each having four equivalent positions in the crystallographic unit cell. D5 refers to the fifth Fe site having point symmetry *1* and eight equivalent positions in the unit cell.

Parameter	D1	D2	D3	D4	D5
δ (mm/s)	0.37	0.33	0.38	0.38	0.40
ΔE_Q (mm/s)	0.70	−0.74	0.20	0.15	0.86
RA	1/6	1/6	1/6	1/6	2/6

A fit of the experimental spectrum using five doublets with respective parameter values as predicted by the DFT model, was found to have still too many degrees of freedom to converge to an acceptable result. As can be noticed from Table 2, doublets D1 and D2 are expected to exhibit very similar parameter values, and so do doublets D3 and D4. Therefore, one single doublet, D12, was taken to represent doublets D1 and D2, and another doublet, D34, to account for doublets D3 and D4. As such, and presuming that no texture effects are relevant, the ILEEMS spectrum of the θ-layer was analyzed using three symmetric doublets D12, D34 and D5, each showing independent ΔE_Q, δ and Γ (line width) parameters, but all three with an equal relative area (*RA*) as required by the number of equivalent sites for the distinct Fe sites in the crystallographic unit cell. This approach still did not lead to a satisfactory fit, the line width parameter of one of the doublets having been adjusted to a value significantly narrower than the instrumental width (~0.25 mm/s). Therefore, in a next stage of the data analysis the line widths of all three doublets were imposed to take the same value, as there is no plausible reason why they should be significantly different. This additional constraint produced an adequate fit, the numerical

Table 3
Mössbauer parameters of the quadrupole doublets (D12, D34 and D5) resolved from the spectrum of the θ-layer, as determined by the present analysis. δ: center shift; ΔE_Q: quadrupole splitting; Γ: full line width at half maximum; *RA*: relative area. Error values are given between brackets.

Parameter	D12	D34	D5
δ (mm/s)	0.218(5)	0.211(5)	0.200(5)
ΔE_Q (mm/s)	0.354(5)	0.093(5)	0.499(5)
Γ (mm/s)	0.246(5)	0.246(5)	0.246(5)
RA	2/6	2/6	2/6

results of which are listed in Table 3. The as-such calculated spectrum, as well as the three resolved doublet components are reproduced in Fig. 6.

Several attempts to analyze the ILEEMS spectrum of the θ-layer using other constraints were also carried out, some yielding slightly better goodness-of-fit values, however, commonly resulting in too narrow line widths for one or more of the doublets, and hence to be regarded unrealistic. The results in Fig. 6 and Table 3 are therefore believed to be a site-resolved experimental analysis of the Mössbauer spectrum of Fe_4Al_{13}, guided by DFT predictions and consistent with the crystallographic structure of this material. This goes beyond the phenomenological characterizations that were so far available in the literature [25,28].

To summarize, taking into account the totality of the information drawn from various complimentary techniques such as EBSD, XRD, ILEEMS and DFT, it may affirmatively be concluded that the θ-layer, which is observable in Fig. 2, really is a Fe_4Al_{13} phase with the crystal structure as determined by Grin et al. [22].

4.3.2. ILEEMS on the sample with exposed η-layer

Figs. 7 and 8 present the experimental and adjusted ILEEMS spectra for the η-layer, the latter ones according to different fitting models as described hereafter. The experimental spectrum shows a doublet shape, however clearly asymmetric, and is considerably different from the spectrum in Fig. 6, thus confirming that the composition of the involved layer differs from that of the θ-phase. In the following section, three different approaches are discussed that were attempted to fit the experimental spectrum.

According to the Wyckoff site assignment by Burkhardt et al. [3], Fe occupies only one type of position in the Fe_2Al_{5+x} crystal, in casu the 4c site. However, this is only correct in an average sense, when the partially occupied Al-8f and Al-4b are considered as being occupied by effective atoms that are a mixture of Al atoms and vacancies. In reality, there is either a full Al atom or a full vacancy on every position, without long-range order. This leads to the appearance of a large distribution of possible co-ordinations for the Fe atoms, and therefore to a distribution of Mössbauer parameters. Hence, a certain quadrupole splitting distribution may be reflected in the observed spectrum. Therefore, in a first analysis approach, the ILEEMS spectrum was numerically analyzed by a model-independent quadrupole splitting distribution, for which the calculated spectrum consisted of a number of doublets with equally spaced quadrupole splittings ΔE_Q in the range 0.0–0.9 mm/s and with the line widths of the elemental doublet components all fixed at the value of the instrumental line width as determined by the calibration. In first approximation, the center shifts δ were forced to be equal for all elemental doublets. This approximation is corroborated by subsequent fitting approaches presented below. Further, it was experienced that a significantly better goodness-of-fit value (χ^2) was obtained for an adjustment using an asymmetric doublet line intensity, assumed to be the same for all elemental doublets. The occurrence of asymmetry of the emission lines is clearly noticeable in the raw experimental ILEEMS spectrum depicted in Fig. 7 and may be ascribed to texture effects. In the absence of preferential orientation of the electric field gradient (EFG) acting at the probe ^{57}Fe nuclei in the sample (i.e. no texture), a doublet arising from one particular Fe site should be symmetric, i.e.,

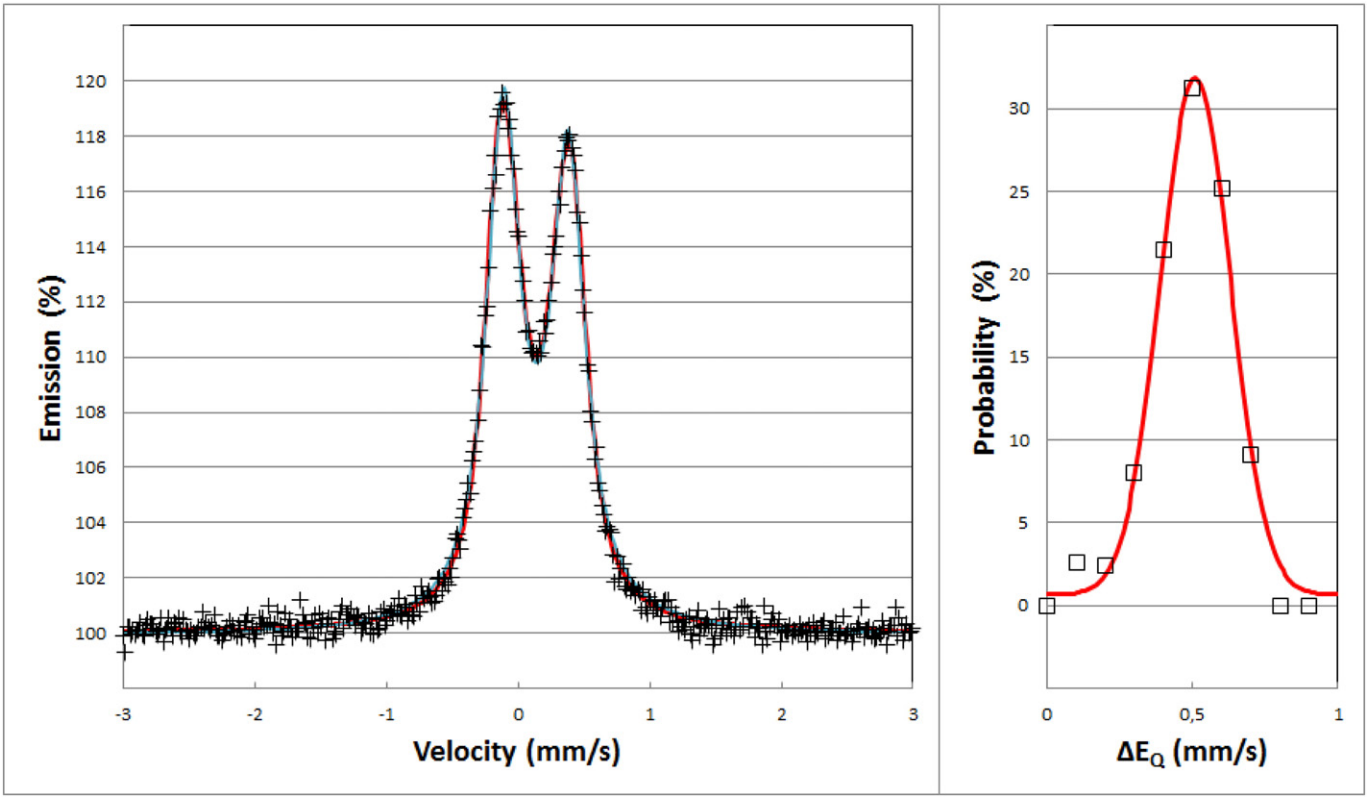

Fig. 7. Left: experimental (crosses) and calculated ILEEMS spectra for the η-layer according to a quadrupole splitting distributed component adjustment (red solid line) and to a one-doublet adjustment (blue solid line). Mössbauer parameters are given in Table 4. Right pane: evaluated distribution profile (squares) of the quadrupole splitting (ΔE_Q) as determined from the analysis of the ILEEMS spectrum using a model-independent quadrupole splitting distribution, and related adjusted Gaussian curve (red solid line) of which the parameters are cited in text.

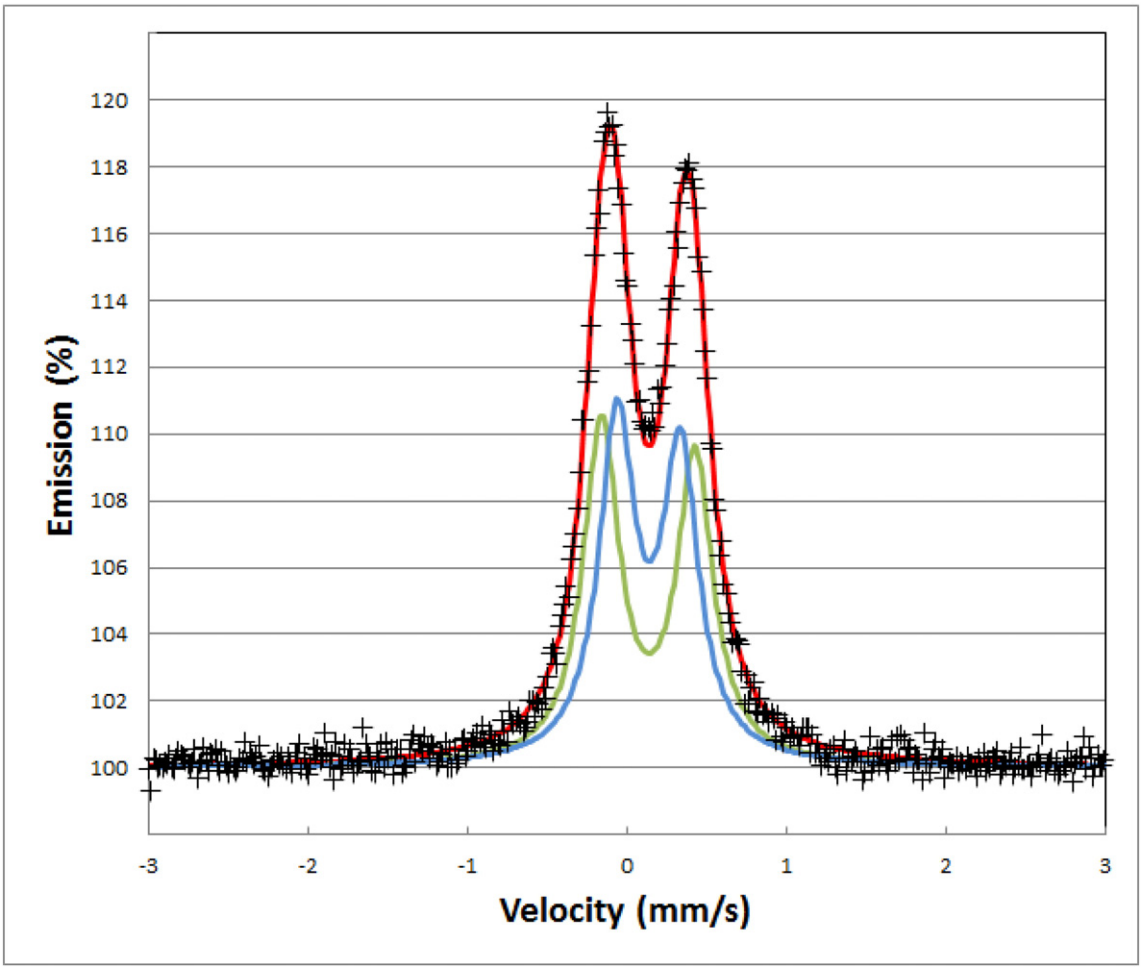

Fig. 8. Experimental (crosses) and calculated (solid red line) ILEEMS spectra for the η-layer according to a two-doublet adjustment. Doublet parameters are given in Table 4.

with equal line intensities and equal line widths for the low- and high-velocity absorption/emission lines of the doublet spectrum. The appearance of texture effects in the η-layer is not fully unexpected, since it has been shown [1] that the [001] crystallographic direction in the η-layer is favored. This feature was more recently confirmed by EBSD observations [53] and, in the present sample, can be expected on the basis of the EBSD mapping in Fig. 3, showing the presence of columnar η-layer grains with the c-axis oriented parallel to the direction perpendicular to the rolling plane of the steel substrate. This preferential orientation gives rise to texture effects and hence may explain the observed asymmetry in the individual line intensities of the doublets in the ILEEMS spectrum.

Accounting for the presence of texture effects, thereby assuming that the extent of asymmetry in line intensities is equal for all elemental doublet contributions to the ΔE_Q distribution, the experimental line shape could be adequately reproduced (solid line in Fig. 7) with adjusted parameter values (referring to highest probability in the distribution) as indicated in Table 4. In order to assess the variance of the ΔE_Q distribution, a Gaussian curve was adjusted to the evaluated ΔE_Q distribution profile, yielding a mean value of ca. 0.51 mm/s and a standard deviation (σ) of ca. 0.12 mm/s. The results of this fitting approach thus demonstrate that the experimental spectrum is consistent with the presence of a multitude of Fe co-ordinations. The rather narrow and symmetric distribution profile of ΔE_Q, however, is an indication that these different co-ordinations have but a small effect on the hyperfine interactions of the probe ^{57}Fe nuclei.

In a second trial to analyze the experimental spectrum of the η layer, the ordered model for Fe_2Al_{5+x} that is described in the earlier section "Sample production, experimental and computational procedures" was considered. This model samples the global distribution of possible Fe co-ordinations in Fe_2Al_{5+x} by only two distinct Fe sites. It cannot be known whether the ΔE_Q values of the two related doublets in the ILEEMS spectrum are near the center or near the tails of the ΔE_Q distribution, which makes the uncertainty on these predictions larger than for the θ-layer. However, this model suggests that the average quadrupole splitting in the η-layer is most likely larger than the quadrupole

Table 4
Mössbauer parameters of the subspectra resolved from the η-layer spectrum following a two-doublet, a quadrupole splitting distributed component and an one-doublet adjustment. (LLI and RLI: left- and right-line intensity of a doublet subspectrum, respectively). δ: center shift; ΔE_Q: quadrupole splitting; Γ: full line width at half maximum; *RA*: relative area. D1 and D2: doublets in the two-doublet adjustment. Error values are given between brackets. *: highest probability value.

	DFT predictions		two-doublet adjustment		distributed component adjustment	one-doublet adjustment
	D1	D2	D1	D2		
δ (mm/s)	0.46	0.43	0.243(5)	0.246(5)	0.243(5)	0.243(5)
ΔE_Q (mm/s)	1.21	0.99	0.59(1)	0.40(1)	0.51(1)*	0.494(5)
Γ (mm/s)			0.275(10)	0.275(10)	0.253	0.309(5)
LLI:RLI			1:0.905	1:0.905	1:0.912	1:0.910
RA	0.500	0.500	0.500	0.500	1	1

splittings in the θ-layer. A fitting approach that directly mimics this model crystal, has two equally populated but differently positioned doublet contributions (see Table 4). Thus, the ILEEMS spectrum of the presumed η-layer was analyzed assuming two doublets with equal relative areas *(RA)* and equal line widths (*Γ*). As for the earlier distribution fit, a better χ^2 value was obtained for an adjustment with asymmetric line intensities for the individual low- and high-velocity components constituting the doublets. The numerical results following this approach are also presented in Table 4. It should be noted at this point that the adjusted δ values for the two doublets are equal within experimental error limits. Fig. 8 shows in solid lines the as-such calculated total spectrum and the two resolved individual doublets.

Both the first (model-independent ΔE_Q distribution) and the second (superposition of two discrete asymmetric doublets) fitting procedure show that the difference in parameters for the doublets corresponding to presumably different Fe co-ordinations are rather small, which makes it plausible that a one-doublet fit of the experimental η-ILEEMS spectrum would also be adequate. This simple model is indeed what has been adopted in the earlier literature [27,28,29]. In order to check consistency of the present experimental data with that earlier reported work, a third analysis of the spectrum of the present η-layer was made, assuming one doublet with equal line widths, but with unequal line intensities for the individual lines because of the texture effect. The as-such calculated spectrum is also shown in Fig. 7 (blue solid line). The adjusted Mössbauer parameter values resulting from this single-doublet fit (see Table 4) are in line with the results reported by Prudêncio et al. [28] and are very similar to the values found by Fedotova et al. [27] and Avettand et al. [29].

Table 4 summarizes the results for these three types of analysis applied in this work to interpret the ILEEMS spectrum of the η phase. It is noticed that the quadrupole splitting for the one-doublet fit is close to the average of the two values for the two-doublet fit and to the maximum-probability quadrupole splitting of the evaluated ΔE_Q-distribution. Further, the two ΔE_Q values adjusted in the two-doublet fit are also within the one-σ range around the mean value of the presumed Gaussian ΔE_Q-distribution. The differences for the respective center shift values are considered to be insignificant, as well as the differences in the asymmetry of the line intensities. The line width obtained for the two-doublet fit is somewhat smaller than the value derived for the single-doublet fit, but both are slightly higher than the instrumental line width, as can be expected. However, because the two-doublet adjustment combined with the DFT results and the ΔE_Q distribution model both yield clearly better goodness-of-fit values (χ^2) compared to the one-doublet fit (13% and 24% respectively), the various above described analysis trials corroborate the interpretation that the observed Mössbauer spectrum of the present η-layer is actually the superposition of multiple doublets, related to different Fe co-ordinations in the structure. The results obtained from EBSD, XRD, APT, ILEEMS and DFT therefore favor Fe_2Al_{5+x} as being the composition of the η-layer with the structure as described by Burkhardt et al. [3].

5. Conclusion

The intermetallic layers appearing in a hot-dip Al-coated steel substrate were identified and characterized unambiguously by EBSD, XRD, APT, ILEEMS and DFT.

The top-most intermetallic layer (θ), just beneath the Al cover layer of the hot-dip Al-coated specimen, was identified as being Fe_4Al_{13} by EBSD, XRD and APT. DFT calculations showed the stability of the Fe_4Al_{13} phase and predicted Fe_4Al_{13} to be the only stable composition in that area of the Fe-Al phase diagram. Additionally based on the DFT results, the analysis of the ILEEMS spectrum of the layer, was successfully performed in accordance with the crystallographic structure of Fe_4Al_{13}, and consequently for the first time the Mossbauer parameters of the different Fe sites were determined for a physically justified fit model. From these results, it can be concluded that the composition and crystal structure of the θ-layer in hot-dip Al-coated steel is identical to the bulk equilibrium phase known as Fe_4Al_{13}. The common designation "$FeAl_3$" that is often used to refer to this phase is misleading, and use of this notation should be abandoned in favor of Fe_4Al_{13}.

Concerning the second intermetallic layer (η) just underneath the Fe_4Al_{13} layer of the present HDA steel, the findings of EBSD, XRD and APT support the description of the crystallographic structure of the η-phase by Burkhardt et al. [3]. According to the DFT results, this phase is only slightly metastable in the ground state phase diagram. Its ILEEMS spectrum could be analyzed by a distribution of quadrupole splittings, due to a variety of Fe co-ordinations, consistent with the composition and partially disordered structure of the η-phase following [3]. This analysis agrees significantly better with the experimental data than a one-doublet fit as was used in earlier studies for this spectrum. Because of the partially disordered structure of the η-phase and the width of its homogeneity region in the Fe-Al diagrams [5,6], the use of Fe_2Al_{5+x} is preferred to refer to the η-layer instead of e.g. Fe_2Al_5.

Acknowledgements

S.C. acknowledges financial support from OCAS NV by an OCAS-endowed chair at Ghent University. All authors gratefully acknowledge OCAS NV for providing materials and technical support.

Appendix A. Supplementary data

Supplementary data to this article can be found online at http://dx.doi.org/10.1016/j.surfcoat.2017.05.091.

References

[1] T. Heumann, S. Dittrich, Uber die Kinetik der Reaktion von festem und flüssigem aluminium mit Eisen, Z. Met. 50 (1959) 617–625.
[2] K. Schubert, Weitere Beispiele für die Ortskorrelation der Außenelektronen in Kristallen, Z. Met. 44 (1953) 254.
[3] U. Burkhardt, Y. Grin, M. Ellner, K. Peters, Structure refinement of the iron-aluminium phase with the approximate composition Fe_2Al_5, Acta Cryst B50 (1994) 313–316.
[4] S. Kobayashi, T. Yakou, Control of intermetallic compound layers at interface between steel and aluminum by diffusion-treatment, Mater. Sci. Eng. A 338 (1) (2002) 44–53.
[5] X. Li, A. Scherf, M. Heilmaier, F. Stein, The Al-rich part of the Fe-Al phase diagram, J. Phase Equilib. Diffus. 37 (2016) 162–173.
[6] K. Han, I. Ohnuma, R. Kainuma, Experimental determination of phase equilibria of Al-rich portion in the Al-Fe binary system, J. Alloys Compd. 668 (2016) 97–106.
[7] V. Jindal, V.C. Srivastava, A. Das, R.N. Ghosh, Reactive diffusion in the roll bonded iron–aluminum system, Mater. Lett. 60 (13–14) (2006) 1758–1761.
[8] Y. Tanaka, M. Kajihara, Morphology of compounds formed by isothermal reactive diffusion between solid Fe and liquid Al, Mater. Trans. 50 (9) (2009) 2212–2220.
[9] N. Takata, M. Nishimoto, S. Kobayashi, M. Takeyama, Morphology and formation of Fe–Al intermetallic layers on iron hot-dipped in Al–Mg–Si alloy melt, Intermetallics 54 (2014) 136–142.
[10] N. Takata, M. Nishimoto, S. Kobayashi, M. Takeyama, Crystallography of Fe_2Al_5 phase at the interface between solid Fe and liquid Al, Intermetallics 67 (2015) 1–11.
[11] S.Y. Rodriguez, X. Zheng, J.H. Ross Jr., Computational study of magnetic and vibrational properties of Fe_4Al_{11-x} and Fe_4Al_{11-y} Zny, IEEE Trans. Magn. 47 (10) (2011) 2924–2927.
[12] P. Matysik, S. Jóźwiak, T. Czujko, Characterization of low-symmetry structures from phase equilibrium of Fe-Al system—microstructures and mechanical properties, Materials 8 (2015) 914–931.
[13] G. Eggeler, W. Auer, H. Kaesche, Reactions between low alloyed steel and initially pure as well as iron-saturated aluminium melts between 670 and 800 degree C, Z. Met. 77 (1986) 239–244.
[14] M. Hirai, T. Sato, G. Ohira, Interfacial stability of α(Al-rich solid solution)-liquid interface of unidirectionally solidified Al-FeAl3 eutectic alloy, J. Cryst. Growth 38 (1977) 340–352.
[15] P. Skjepre, An electron microscopy study of the phase Al_3Fe, J. Microsc. 148 (1987) 33–50.
[16] R.K. Davies, V. Randle, G.J. Marshall, Continuous recrystallization—related phenomena in a commercial Al–Fe–Si alloy, Acta Mater. 46 (17) (1998) 6021–6032.
[17] P.G. Gonzales-Ormefio, H.M. Petrilli, Ab-initio calculations of the formation energies of BCC-based superlattices in the Fe-Al system, Calphad 26 (4) (2002) 573–582.
[18] L. Li, Y. Zhang, C. Esling, H. Jiang, Z. Zhao, Y. Zuoa, J. Cui, Crystallographic features of the primary Al_3Fe phase in as-cast Al–3.31wt% Fe alloy, J. Appl. Crystallogr. 43 (2010) 1108–1112.
[19] E. Pochec, S. Józwiak, K. Karczewski, Z. Bojar, Maps of Fe–Al phases formation kinetics parameters during isothermal sintering, Thermochim. Acta 545 (2012) 14–19.

[20] C.-H. Zhang, S. Huang, J. Shen, N.-X. Chen, Structural and mechanical properties of Fe–Al compounds: an atomistic study by EAM simulation, Intermetallics 52 (2014) 86–91.
[21] P.J. Black, The structure of $FeAl_3$, Acta Cryst 8 (1955) 43.
[22] J. Grin, U. Burkhardt, M. Ellner, K. Peters, Refinement of the Fe_4Al_{13} structure and its relationship to the quasihomological homeotypical structures, Z. Krist. 209 (1994) 479–487.
[23] U.R. Kattner, Al-Fe phase diagram, in: T.B. Massalski, H. Okamoto, P.R. Subramanian, L. Kacprzak (Eds.), Binary Alloy Phase Diagrams, 2nd editionASM International, Materials Park, OH 1990, p. 147.
[24] O. Kubaschewski, Iron — Binary Phase Diagrams, Springer, Berlin Heidelberg, 1982.
[25] M. Turchanin, N. Kolchugina, A. Watson, A. Kroupa, Al-Fe Binary Phase Diagram Evaluation, MSI EurekaEvaluation Report 20.10236.1.8 MSI Materials Science International Services GmbH, Stuttgart, 2014.
[26] R.S. Preston, R. Gerlach, Mössbauer effect in dilute alloys of iron in aluminum, Phys. Rev. B Solid State 3 (5) (1971) 1519–1526.
[27] J. Fedotova, A. Ilyuschenko, T. Talako, A. Belyaev, A. Letsko, A. Zalesskii, J. Stanek, Phase and Structural Transformations in Fe_xAl_{1-x} Powder Alloys Studied by ^{57}Fe Mössbauer Spectroscopy and XRD, AIP Conf. Proc. 765 (2005) 317–321.
[28] L.M. Prudêncio, I.D. Nogueira, J.C. Waerenborgh, A.P. Gonçalves, O. Conde, Formation of Al–Fe surface alloys by ion implantation of Fe in Al, Surf. Coat. Technol. 158–159 (2002) 339–342.
[29] M.N. Avettand-Fènoël, C. Cordier-Robert, G. Guillemot, F. Goodwin, J. Foct, Feature of solid-liquid metals reaction revealed by conversion electron Mössbauer spectroscopy, Hyperfine Interact. 90 (1–3) (2009) 211–218.
[30] B. Lemmens, H. Springer, M.J. Duarte, I. De Graeve, J. De Strycker, D. Raabe, K. Verbeken, Atom probe tomography of intermetallic phases and interfaces formed in dissimilar joining between Al alloys and steel, Mater. Charact. 120 (2016) 268–272.
[31] V. Randle, O. Engler, Introduction to Texture Analysis: Macrotexture, Microtexture and Orientation Mapping, CRC Press, Boca Raton, 2000.
[32] E. De Grave, R. Vandenberghe, C. Dauwe, ILEEMS: methodology and applications to iron oxides, Hyperfine Interact. 161 (1–4) (2005) 147–160.
[33] G. Hautier, S. Ping Ong, A. Jain, C.J. Moore, G. Ceder, Accuracy of density functional theory in predicting formation energies of ternary oxides from binary oxides and its implication on phase stability, Phys. Rev. B 85 (2012) 155208.
[34] J.E. Saal, S. Kirklin, M. Aykol, B. Meredig, C. Wolverton, Materials design and discovery with high-throughput density functional theory : the open quantum materials database, J. Mater. 65 (2013) 1501.
[35] K. Lejaeghere, V. Van Speybroeck, G. Van Oost, S. Cottenier, Error estimates for solid-state density-functional theory predictions: an overview by means of the ground-state elemental crystals, Crit. Rev. Solid State Mater. Sci. 39 (2014) 1.
[36] A.M. Deml, R. O'Hayre, C. Wolverton, V. Stevanovic, Predicting density functional theory total energies and enthalpies of formation of metal-nonmetal compounds by linear regression, Phys. Rev. B 93 (2016), 085142.
[37] L. Errico, K. Lejaeghere, J. Runco, S.N. Mishra, M. Renter, S. Cottenier, Precision of electric-field gradient predictions by density functional theory and implications for the nuclear quadrupole moment and its error bar of the ^{111}Cd 245 keV $5/2^+$ level, J. Phys. Chem. C 120 (40) (2016) 23111–23120.
[38] S. Curtarolo, D. Morgan, G. Ceder, Accuracy of ab initio methods in predicting the crystal structures of metals: a review of 80 binary alloys, CALPHAD: Comput. Coupling Phase Diagrams Thermochem. 29 (2005) 163–211.
[39] M. Mihalkovic, M. Widom, Structure and stability of Al_2Fe and Al_5Fe_2: first-principles total energy and phonon calculations, Phys. Rev. B 85 (2012), 014113.
[40] P. Dufek, P. Blaha, K. Schwarz, Determination of the nuclear quadrupole moment of ^{57}Fe, Phys. Rev. Lett. 75 (1995) 3545–3548.
[41] A. Svane, N.E. Christensen, C.O. Rodriguez, M. Methfessel, Calculations of hyperfine parameters in tin compounds, Phys. Rev. B 55 (1997) 12572–12577.
[42] G. Dénès, M.C. Madamba, H. Merazig, A. Muntasar, at HYPERFINE2016, http://www.hyperfine2016.be/video/4.
[43] B. Lemmens, Y. Gonzalez Garcia, B. Corlu, J. De Strycker, I. De Graeve, K. Verbeken, Surf. Coat. Technol. 260 (2014) 34–38.
[44] G.S. Pawley, Unit-cell refinement from powder diffraction scans, J. Appl. Crystallogr. 14 (1981) 357–361.
[45] E. Sjöstedt, L. Nordström, D.J. Singh, An alternative way of linearizing the augmented plane-wave method, Solid State Commun. 114 (2000) 15–20.
[46] G.K.H. Madsen, P. Blaha, K. Schwarz, E. Sjöstedt, L. Nordström, Efficient linearization of the augmented plane-wave method, Phys. Rev. B 64 (2001) 195134.
[47] S. Cottenier, Density Functional Theory and the Family of (L)APW Methods: a Step-by-step Introduction, Instituut voor Kern- en Stralingsfysica, KULeuven, Belgium, 2002 freely available from http://www.wien2k.at/reg_user/textbooks].
[48] P. Blaha, K. Schwarz, G. Madsen, D. Kvasnicka, J. Luitz, WIEN2k, an Augmented Plane Wave + Local Orbitals Program for Calculating Crystal Properties (Karlheinz Schwarz, Techn), Universität Wien, Austria, 1999.
[49] J.P. Perdew, K. Burke, M. Ernzerhof, Generalized gradient approximation made simple, Phys. Rev. Lett. 77 (1996) 3865–3868.
[50] W.-J. Cheng, C.-J. Wang, Growth of intermetallic layer in the aluminide mild steel during hot-dipping, Surf. Coat. Technol. 204 (2009) 824–828.
[51] A. Bouayad, C. Gerometta, A. Belkebir, A. Ambari, Kinetic interactions between solid iron and molten aluminum, Mater. Sci. Eng. A363 (2003) 53–61.
[52] A. Canakci, F. Erdemir, T. Varol, S. Ozkaya, H. Mindivan, Microstructure and properties of Fe-Al intermetallic coatings on the low carbon steel synthesized by mechanical alloying, Int. J. Adv. Manuf. Technol. 73 (5–8) (2014) 849–858.
[53] I. Infante Danzo, Y. Houbaert, K. Verbeken, Diffusion driven columnar grain growth induced in an Al–Si-coated steel substrate, Surf. Coat. Technol. 251 (2014) 15–20.